# Supplementary Information for

# Foliar Graphene Sensor for Continuous, Non-Destructive Monitoring of Plant Tissue Hydration, Drought Stress and Circadian Rhythm

Ning Liu[1], Pascal Mahukpe Ayelo[2,*], Utkarsh Misra[1,*], Maria Lynn Ulatowski[3], Caixing Xiong[2], Neelotpala Kumar[1], Michael Kolomiets[2], Henry Fadamiro[2], Jean Anne Incorvia[1], Ashley M. Matheny[3], Dmitry Kireev[4,&], and Deji Akinwande[1,5,&]

[1] Department of Electrical and Computer Engineering, University of Texas at Austin, Austin, Texas 78712, USA
[2] Department of Entomology, Texas A&M University, College Station, TX 77843
[3] Department of Earth and Planetary Sciences, The University of Texas at Austin, Austin, Texas 78712, USA
[4] Department of Biomedical Engineering, University of Massachusetts Amherst, Amherst, MA 01002, USA
[5] Department of Biomedical Engineering, University of Texas at Austin, Austin, Texas 78712, USA

[*] These authors contributed equally

[&] Corresponding authors: deji@ece.utexas.edu and dkireev@umass.edu

## Supplementary Note 1. Comparison of Plant Water Content Monitoring Techniques

Accurate measurement of plant water status is essential for understanding plant physiology and improving irrigation management. Traditionally, leaf water content (LWC) has been quantified using destructive gravimetric methods, in which leaves are excised and dried to determine water loss. Although highly accurate, such approaches cannot provide continuous measurements and are unsuitable for in situ monitoring in natural environments.

To address this limitation, recent studies have developed field-deployable sensors that estimate plant hydration indirectly by measuring environmental parameters near the leaf surface, such as relative humidity or vapor pressure deficit, using resistance-, capacitance-, or voltage-based sensors[1–3]. Even though these sensors provide a good estimate of tangential hydration features such as relative humidity, they typically infer leaf hydration indirectly from surrounding microclimate conditions rather than measuring the internal water status of the leaf itself. In addition to the derived measurements, many of these systems utilize graphene oxide (GO)[1,4–6] or laser-induced graphene (LIG) films as the sensing material (Table S1)[3,7]. Because these sensors are intended for field deployment, minimizing interference with natural leaf physiology is essential. However, many reported designs, particularly those based on GO or LIG films, partially block light transmission and restrict gas exchange when attached to the leaf surface, which may perturb plant physiology and limit their suitability for long-term monitoring. In addition, most reported systems are configured to measure surface humidity rather than internal leaf hydration, which can introduce delays or indirect responses relative to physiological water dynamics.

Alternative non-contact approaches, including terahertz (THz) wave propagation and quantum cascade laser techniques, have demonstrated the ability to probe internal leaf hydration and pressure–volume relationships[8,9]. Although these optical methods provide valuable mechanistic insights, they typically rely on bulky and costly instrumentation and are therefore less practical for continuous in-field monitoring.

The foliar graphene sensor (FGS) developed in this work addresses these challenges by directly probing leaf hydration through four-probe bioimpedance measurements. In this configuration, the excitation current passes through the leaf tissue itself, enabling interrogation of internal hydration dynamics rather than relying on surface or environmental proxies. The four-probe configuration minimizes the influence of contact resistance and parasitic impedance, allowing accurate extraction of tissue impedance values[10,11]. Because the measurement current flows through the leaf tissue, the resulting impedance signal reflects the electrical properties of the plant tissue and therefore provides a direct indicator of leaf hydration state. In addition, the ultrathin and lightweight graphene-based sensing interface enables continuous operation for more than two weeks without restricting leaf growth, outperforming many GO- and LIG-based alternatives in both physiological compatibility and operational duration. In addition, the FGS platform can be directly deployed under natural environmental conditions. Although outdoor measurements exhibit slightly higher signal variability than controlled laboratory experiments, the raw (unfiltered) data still clearly resolve variations in hydration states and diurnal physiological dynamics (Figure 5e). Furthermore, optical techniques such as THz spectroscopy are typically performed as discrete spot measurements rather than continuous monitoring. Compared with these approaches, the system presented here provides a portable, low-cost, and scalable sensing platform capable of real-time, long-term monitoring while maintaining minimal interference with plant physiology. By combining direct tissue-level hydration sensing with a mechanically compliant and wearable device architecture, the FGS platform enables practical and continuous monitoring of plant water status in both controlled and field environments.

## Supplementary Note 2. Electrode Architecture and Mechanical Integration of the Foliar Graphene Sensor (FGS)

Establishing a mechanically compliant and non-perturbative interface between electronic devices and living leaves presents a significant challenge due to the softness, continuous growth, and dynamic motion of plant tissues. The electrode architecture of the FGS was therefore designed to minimize mechanical stress, preserve natural leaf movement, and ensure stable electrical contact.

The FGS employs bilayer graphene as the sensing electrode. Although graphene possesses exceptional intrinsic mechanical strength, its atomic-scale thickness makes it mechanically fragile and difficult to handle. To provide mechanical integrity and ease of handling, an ultrathin polymethyl methacrylate (PMMA) support layer was incorporated (Figure S5). The resulting graphene–PMMA laminate forms a conformal electrode that directly interfaces with the leaf surface.

Electrical connection between the sensing electrode and the measurement instrumentation was achieved using ultrathin gold tape fabricated by depositing a conductive gold layer onto a flexible polymer substrate. Owing to its minimal thickness and high flexibility, the gold tape exhibits mechanical compliance comparable to the graphene–PMMA laminate, thereby minimizing stress concentration at the junction and preventing mechanical failure during leaf movement.

Although gold provides excellent electrical conductivity, the extremely small thickness of the gold tape leads to increases resistance over long connection lengths. To ensure reliable signal transmission while preserving flexibility, silver epoxy was used to bond the terminal end of the gold tape to an enameled copper wire, which then interfaced with the measurement instrument.

To minimize mechanical loading on the leaf, a 36 AWG enameled copper wire was selected due to its ultralight weight (0.116 g/m) and small diameter (0.14 mm). Conventional electrical leads and alligator clips were found to impose excessive weight, causing leaf bending and restricting natural diurnal movements, including repositioning and orientation changes. The lightweight wiring configuration enabled stable measurements while preserving natural leaf motion and physiological function.

To quantify the mechanical load imposed by the sensing system, the total mass of the complete setup was measured to be 0.2916 g, including four graphene sensors, four gold tape interconnects, and four connecting wires. The combined mass of the four graphene sensors alone was approximately 0.00035 g (Sartorius Entris II BCE124-1S analytical balance). For comparison, a fully hydrated fifth leaf weighed 6.218 g, indicating that the sensing system accounts for approximately 4.7% of the leaf mass. This minimal mass loading reduces gravitational bending and mechanical perturbation, ensuring unobtrusive monitoring while preserving natural leaf posture, movement, and physiological function.

## Supplementary Note 3. Biocompatibility and Physiological Compatibility of the Foliar Graphene Sensor (FGS)

Maintaining physiological compatibility is essential when interfacing electronic devices with living leaves, as surface coverage may disrupt gas exchange, light transmission, or local tissue function. The FGS was therefore designed to minimize interference with photosynthesis, transpiration, and cellular integrity during prolonged attachment.

More than 20 maize plants were evaluated using the FGS. Across all experiments, no visible chlorosis, lesions, or necrosis were observed in leaf regions covered with the FGS (Figure S1), indicating that prolonged contact does not induce observable tissue stress or damage.

In contrast, mild chlorosis was observed in control regions covered with a non-breathable polymer film. This response is consistent with restricted gas exchange and reduced light transmission, highlighting the importance of breathable and optically transparent interfaces for maintaining leaf physiological function.

The graphene sensing region is ultrathin, optically transparent, and permeable to gas exchange. However, electrical interconnection requires ultrathin gold tape, which is not permeable. To minimize potential physiological interference, the gold tape coverage area was carefully limited during device assembly. The contact area was maintained below 4 mm × 12 mm ($< 0.5$ cm$^2$), thereby minimizing obstruction of gas exchange and light exposure (Figure S1–S4).

After completion of measurements, the FGS was removed by gently wiping the surface with a laboratory tissue (Kimwipes™, Kimtech) moistened with deionized (DI) water, followed by careful peeling of the gold tape. Post-removal inspection revealed no visible differences between previously covered and uncovered regions. The limited gold contact area produced no observable physiological or morphological damage.

Together, these results demonstrate that the FGS provides a physiologically compatible interface with living leaves, enabling prolonged monitoring without compromising tissue integrity or function.

## Supplementary Note 4. Quantification of Leaf Color Difference (Figure 4a)

To quantitatively assess potential color changes between FGS-covered and uncovered leaf regions, digital image analysis was performed to provide an objective measure of visual differences.

Regions of interest (ROIs) were selected using Photoshop (Adobe), excluding major veins to avoid structural artifacts. Mean RGB intensity values were extracted for both covered and uncovered regions.

Color difference was calculated as the Euclidean distance between the mean RGB vectors in three-dimensional color space and normalized to the maximum possible distance within the RGB color cube:

$$\Delta C = \frac{\sqrt{(R_1 - R_2)^2 + (G_1 - G_2)^2 + (B_1 - B_2)^2}}{\sqrt{3 \times 255^2}} \times 100\%$$

R,G,B represent the red, green, and blue intensity values of the selected regions.

This normalized metric provides a quantitative measure of color difference between the two regions, enabling objective evaluation of potential chlorosis or visual tissue changes.

## Supplementary Note 5. Extraction of Impedance Values at Target Frequencies

The raw bioimpedance data consist of frequency-resolved spectra spanning 10 Hz to 100 kHz, sampled at 201 logarithmically spaced frequencies. Each measurement file contains impedance values corresponding to each excitation frequency.

For quantitative analysis and visualization, impedance values at specific target frequencies were extracted from the full spectra. Single-frequency data were used to enable time-series analysis, statistical comparison, and tracking of hydration dynamics.

Target-frequency values (e.g., 1 kHz) were obtained by filtering rows corresponding to the desired excitation frequency and exporting the filtered data for subsequent analysis and plotting.

Data processing was performed using a custom Python script to ensure reproducibility and consistency across datasets.

## Supplementary Note 6. Correlation Analysis Between Impedance and Environmental Variables

To evaluate the relationship between leaf impedance dynamics and environmental conditions, correlation analysis was performed between normalized impedance changes ($\Delta Z/Z_0$ at 1 kHz) and measured environmental parameters(Figure S16).

The analyzed variables included light intensity, soil humidity, ambient temperature, soil electrical conductivity (EC), and relative humidity. Raw datasets were converted to numerical format and cleaned by removing missing values prior to analysis.

Pairwise correlations were quantified using the Pearson correlation coefficient to quantify linear relationships between impedance and environmental variables. The resulting correlation matrix was visualized as a heatmap to facilitate interpretation of multivariate relationships.

Correlation coefficients greater than 0.5 were considered indicative of strong positive correlation, whereas values below -0.5 were considered strongly negative. Intermediate values indicate moderate to weak associations.

All analyses and visualizations were performed using Python (pandas, NumPy, and Seaborn) to ensure reproducibility.

## Supplementary Note 7. Outdoor Environmental Validation

Demonstrating sensor performance under natural environmental conditions is essential for evaluating robustness beyond controlled laboratory settings. Because plants in field environments experience wind-induced motion, fluctuating radiation, and heterogeneous microclimates, outdoor measurements provide a stringent test of sensor stability and physiological relevance.

Outdoor impedance monitoring was conducted on a red oak (*Quercus buckleyi*) (Figure S3), a native woody species, at an experimental agricultural field on the University of Texas at Austin campus (Austin, TX, USA). Plants were exposed to ambient environmental conditions, and impedance and environmental variables were recorded following the protocol described in the main Methods.

Compared with controlled-environment measurements, increased signal variability was observed, reflecting wind-induced motion, environmental fluctuations, and heterogeneous radiation exposure typical of field conditions. Despite this variability, impedance dynamics remained physiologically consistent with environmental drivers, demonstrating the feasibility of outdoor monitoring and supporting cross-species deployment of the foliar graphene sensing platform.

## Supplementary Note 8. Hydration Recovery Dynamics and Coupling with Soil Moisture

Understanding how leaf hydration responds to soil water availability is essential for interpreting plant water status and recovery dynamics. Because water transport occurs through an integrated soil–plant hydraulic continuum, linking leaf impedance measurements to soil moisture dynamics provides validation of the physiological relevance of the sensing platform.

Long-term in situ monitoring of maize leaves enabled quantitative characterization of plant water uptake and recovery dynamics under varying hydration states. Following irrigation, leaf impedance decreased rapidly, indicating immediate water uptake and hydraulic transport from roots to leaf tissues. This initial response typically occurred within approximately 20 minutes, reflecting rapid root–leaf hydraulic connectivity. Impedance then gradually stabilized as tissue hydration approached equilibrium (Figure S11).

Hydration recovery times depended strongly on drought severity. In drought-stressed plants exhibiting visible leaf curling, impedance remained elevated prior to irrigation and declined slowly during recovery, requiring nearly 24 hours to return to baseline levels. This gradual decline coincided with visible physiological recovery, including leaf unfolding and restoration of normal diurnal movement patterns. Such delayed recovery is consistent with previous studies showing that severe or prolonged drought slows restoration of leaf water status and gas exchange[12–15].

In contrast, well-watered plants re-equilibrated much more rapidly after irrigation. Although minor impedance fluctuations occurred due to transient soil moisture variation and internal redistribution of water, impedance stabilized at a fully hydrated state within approximately 5 hours[16] (Figure S11). Under adequate hydration, plants typically require only tens of minutes to a few hours to re-establish water balance, consistent with established plant hydraulic behavior. Recovery time, defined as the interval between irrigation and impedance return to baseline, differed significantly between hydrated and drought-stressed plants, confirming that drought severity strongly influences rehydration kinetics (Figure S12).

Despite differences in recovery timescales, both drought-stressed and well-watered plants exhibited a rapid initial impedance decrease across frequencies following irrigation. In drought-stressed plants, comparable responses at low and high frequencies suggest simultaneous replenishment of extracellular and intracellular water compartments (Figure S10, S15). In well-watered plants, changes were more pronounced at higher frequencies, consistent with rapid intracellular hydration. Over subsequent hours, transient impedance fluctuations likely reflect redistribution of water between extracellular and intracellular spaces, ultimately yielding a uniform hydration profile.

Impedance dynamics also exhibited systematic relationships with soil humidity (Figure S13). During the active recovery phase immediately following irrigation, transient deviations from steady-state behavior were observed; therefore, recovery-phase data were excluded from curve fitting to avoid bias. The remaining data were well described by a logistic relationship ($R^2$ = 0.835), indicating nonlinear coupling between soil moisture availability and leaf hydration state.

This behavior reflects the integrated hydraulic pathway linking soil water availability, root uptake, and tissue hydration.

Together, these observations demonstrate that impedance monitoring captures hydration recovery dynamics and their coupling with soil moisture in real time. The ability to detect early dehydration and track recovery suggests a framework for irrigation management in which watering is triggered before visible stress symptoms emerge, enabling faster recovery and improved water-use efficiency (Figure S14).

## Supplementary Note 9. Hydraulic Coupling Between Sap Transport and Leaf Hydrodynamics

Linking leaf hydration dynamics to whole-plant water transport provides critical insight into how water is redistributed within plants. Because water movement occurs along a continuous soil–plant hydraulic pathway, simultaneous monitoring of sap transport and leaf impedance provides insight into the temporal coordination of water redistribution within the plant.

To quantify stem-level water transport, mini heat field deformation sensors (HFD) based on the design from previous research[15] were used to measure relative sap flux (RSF) in small plants. These mini HFD sensors enable bidirectional sap flow measurements with high temporal resolution through continuous heating and thermocouple-based temperature gradients. The design and calculation of RSF are based on commercially available sensors[17–20]. HFD sensors were designed in kiCad and printed on flexible PCBs (PCB gogo, Shenzhen, Guangdong, China). HFD thermocouples were connected to a datalogger (CR1000x, Campbell Scientific, Logan UT, USA), which recorded temperatures every 30 seconds and averaged them to 30-minute intervals. HFD sensors were placed on the outside of stems below the lowest branching junction. They contain a top, bottom and side thermocouple adjacent to a heating element (SMD 100 ohm resistor) that all make direct contact with the stem when attached. To convert RSF to absolute sap flow (g/h), excised stems were connected to a mass-balance hydraulic conductivity system[15] while a mini HFD sensor was simultaneously applied to the stem to record RSF.

Multi-day averaged diurnal profiles revealed that sap flow is primarily driven by sunlight intensity, exhibiting strong alignment with daily radiation patterns (Figure S17). This behavior reflects transpiration-driven water transport regulated by stomatal conductance and atmospheric demand.

Following irrigation events, sap flow dynamics exhibited a delayed response. Unlike soil moisture, which increases immediately after watering, sap flow peaks typically increased on the following day (Figure S18). This temporal offset indicates that sap transport responds after internal water redistribution and adjustment of transpiration demand rather than directly to soil water availability.

The direct correlation between sap flow and leaf impedance yielded a Pearson correlation coefficient of 0.289 ($p = 3.83 \times 10^{-50}$). Although the correlation strength is modest ($r \approx 0.3$), this is expected because sap flux is governed by multiple interacting environmental and physiological factors, including radiation, vapor pressure deficit, temperature, wind, internal hydration status, and hormonal regulation. Given this complexity, it is unlikely that any single variable fully explains sap flow variance. Thus, the observed correlation strength is reasonable, and the high statistical significance (p-value) indicates a statistically significant relationship despite apparent variability.

Lagged correlation analysis further revealed a temporal offset between sap transport and leaf hydration dynamics. The correlation peaked at approximately 4.5 hours when sap flow was shifted forward relative to impedance, indicating that increases in sap flow precede decreases in leaf impedance (Figure S19). This delay is consistent with the time required for water transported through the xylem to redistribute into leaf tissues and restore cellular hydration. Multiple lag processes coexist in plant water transport. Sap flux is known to lag environmental drivers such as radiation and vapor pressure deficit[21,22], while leaf hydration reflects a later stage of the hydraulic pathway. The observed delay between sap transport and impedance therefore supports the interpretation that impedance measurements capture tissue-level hydration dynamics rather than immediate hydraulic flow.

Together, these observations demonstrate that leaf impedance dynamics are hydraulically coupled to stem sap transport and reflect downstream redistribution of water within plant tissues.

**Figure S1. FGS conformally attached to a corn leaf.** Photograph showing four FGS conformally attached to the adaxial side (top) of a single corn leaf, forming the sensing interface. Gold tape serves as electrical interconnects, and external wires (routed on the backside and not visible) complete the measurement setup.

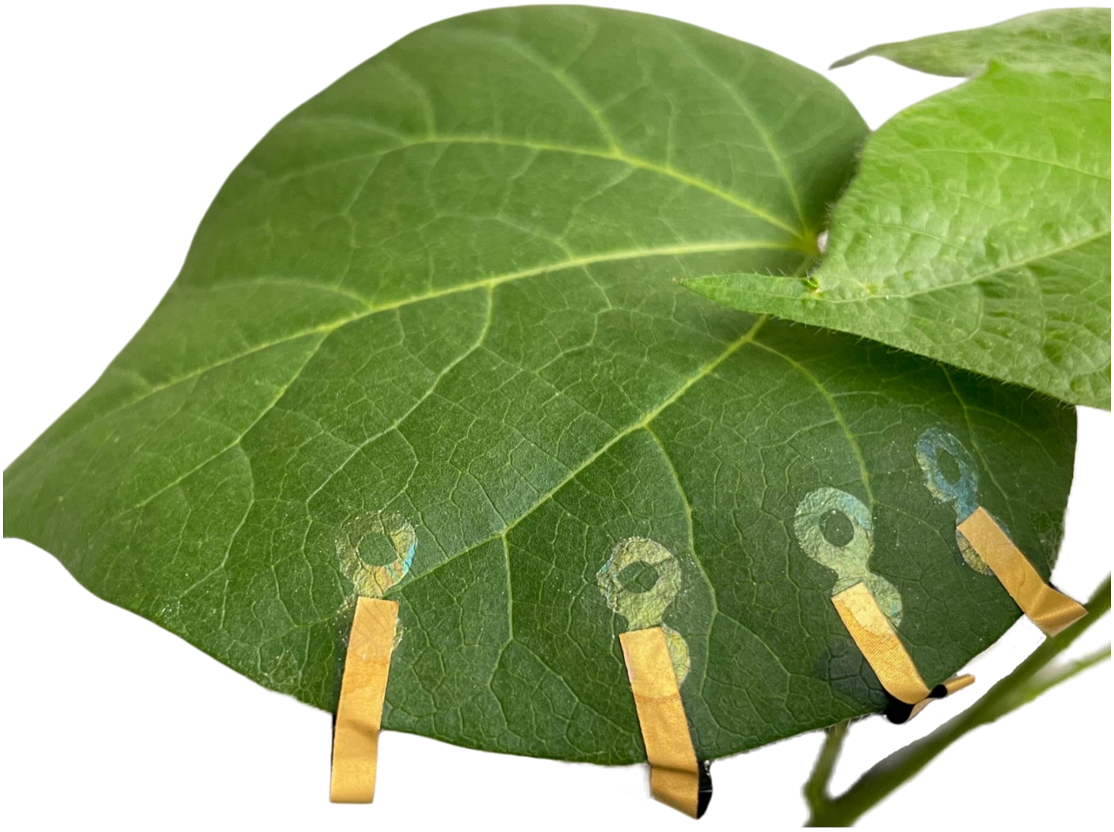

**Figure S2. FGS attached on a cotton leaf.** The sensing configuration shown in Figure S1 is applied to a cotton leaf. Four FGS are attached to the leaf surface and connected via gold adhesive tape to external wiring on the reverse side.

**Figure S3. FGS attached to a red oak (*Quercus buckleyi*) leaf under natural outdoor conditions.** Four FGS are conformally attached to the leaf surface and connected to external wiring using gold tape, following the sensing configuration shown in Figure S1.

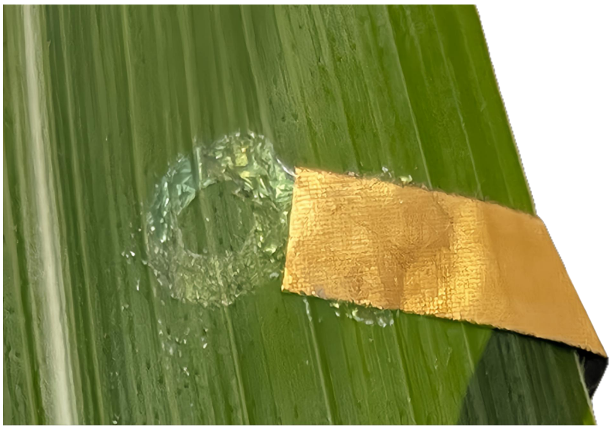

**Figure S4. A single FGS electrode and its electrical interconnect.** Photograph showing a single FGS unit and its gold tape interconnect. The left region of the graphene film contacts the leaf surface, while the right region overlaps the gold tape to form the electrical interconnect.

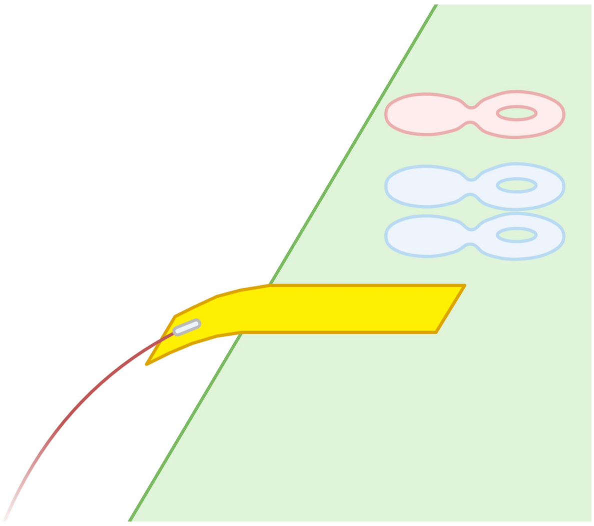

**Figure S5. FGS architecture and measurement configuration.** Schematic illustration of the sensing structure and measurement setup. Pink represents the PMMA supporting layer; blue indicates monolayer graphene; gold corresponds to gold tape; silver denotes silver epoxy; red lines represent enameled copper wires; and green indicates the leaf surface.

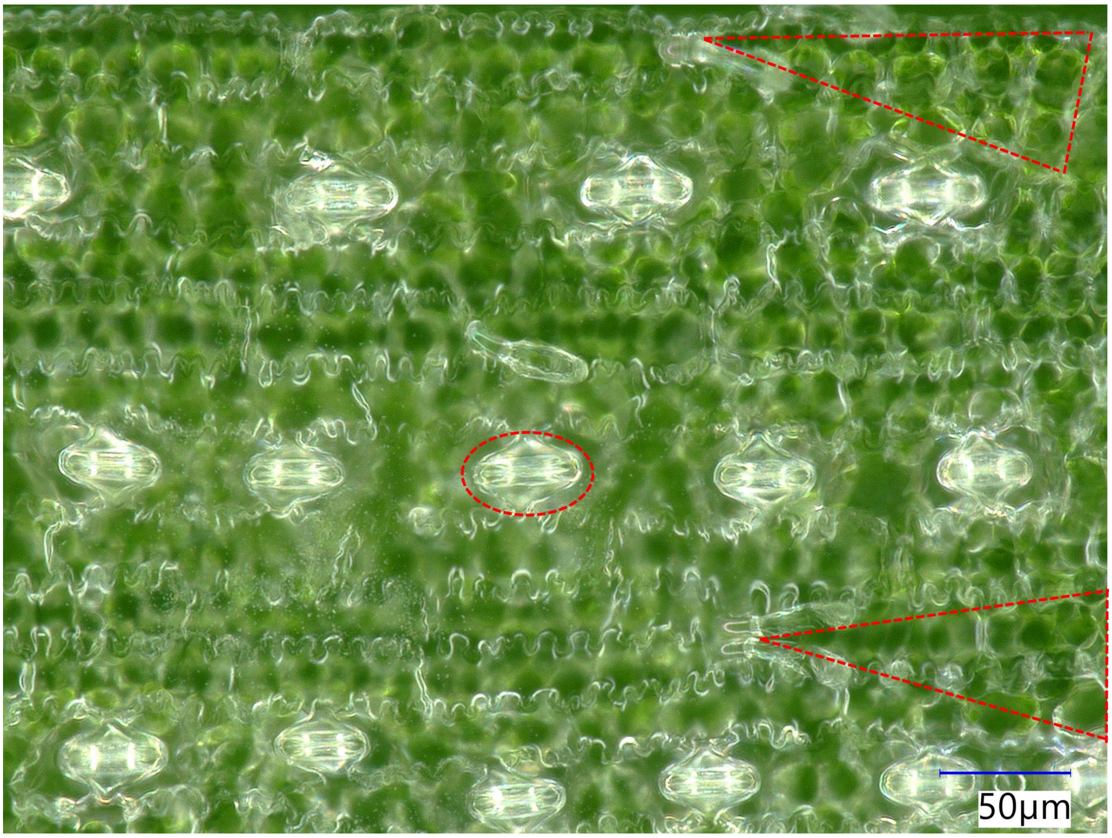

**Figure S6. Microporous structure of the FGS.** Optical micrograph (VHX-X1, Keyance) of an FGS attached to the leaf surface. Triangular micropores in the graphene are outlined with red dashed lines, and a native stomatal pore of the leaf is marked with a red dashed ellipse. Although the graphene micropores do not always align perfectly with the stomata (as shown here), their high density ensures sufficient proximity to allow gas molecules to diffuse through the interfacial gap between the graphene and the leaf surface and enter the micropores, thereby maintaining gas exchange.

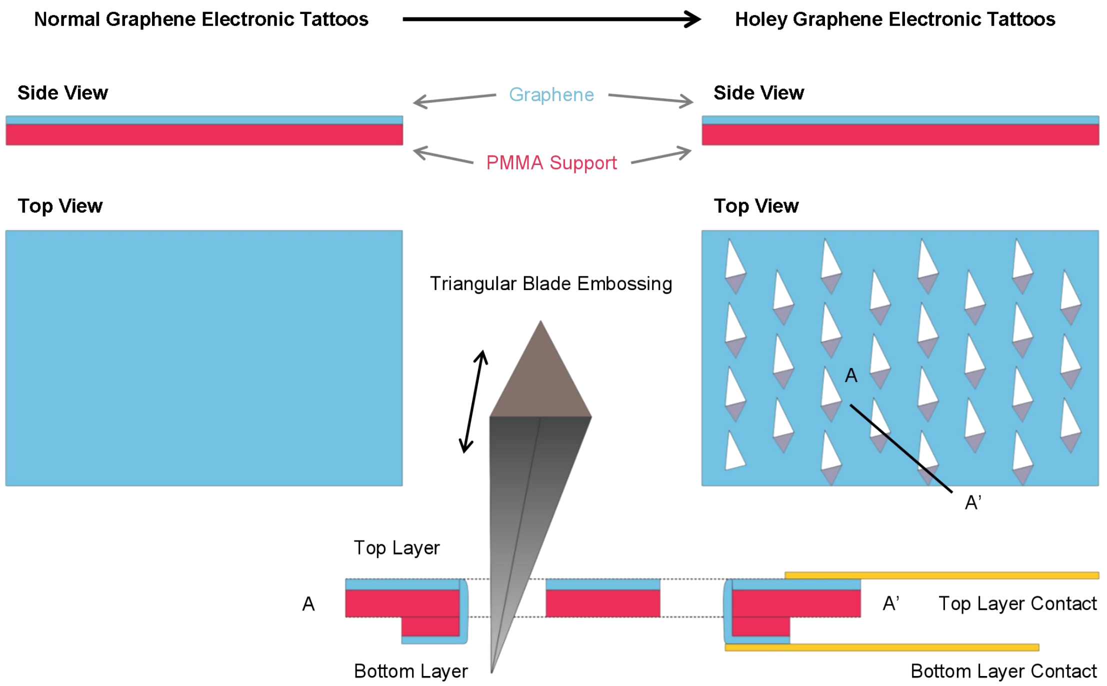

**Figure S7. Formation of triangular micropores on graphene via embossing.** The graphene/PMMA is embossed using a Silhouette Cameo cutter. Because the process involves embossing rather than cutting, the pressed regions adhere to the back side of the film, partially delaminating the graphene and exposing a larger graphene area on the PMMA side. This creates triangular micropores on the graphene surface and enables electrical access to the FGS not only from the top (graphene) surface but also from the bottom (PMMA) side. The detailed fabrication process and electrical characterization of this method have been reported previously[23].

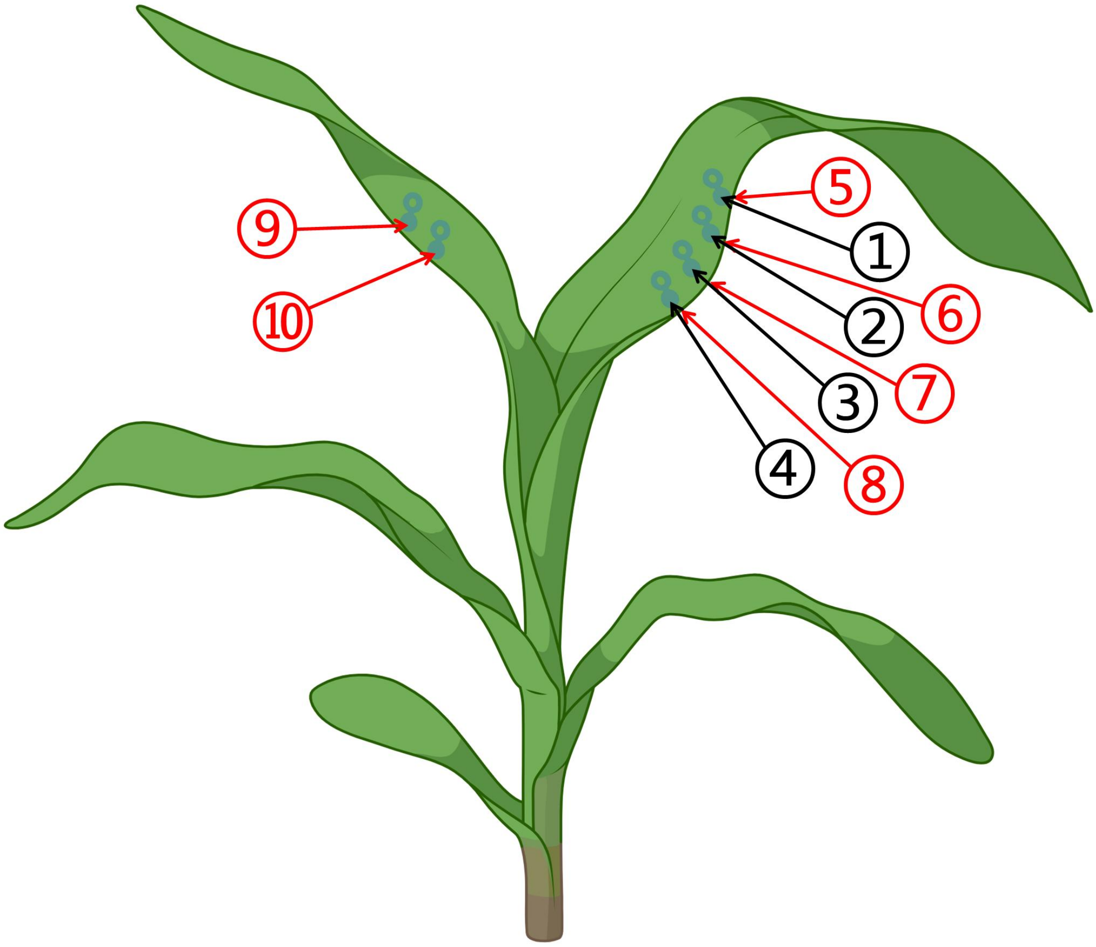

**Figure S8. Placement of FGS on corn leaves.** Black arrows and numbers indicate sensors positioned on the adaxial leaf surface, while red arrows and numbers indicate sensors on the abaxial surface. Sensors 1–4 are placed on the adaxial surface (top), and sensors 5–8 are placed on the abaxial surface (bottom). Sensors 2, 3, 6, and 7 placed on opposite surfaces of the same leaf (across), whereas sensors 6, 7, 9, and 10 are placed on different leaves to measure (between).

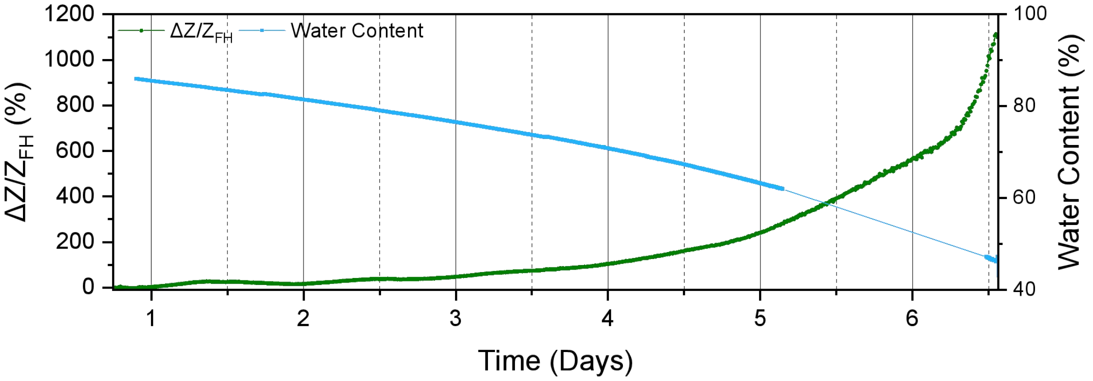

**Figure S9. Correlation between LWC and impedance.** A detached corn leaf was continuously monitored for impedance and weight loss over time. LWC was determined gravimetrically from the fresh and dry weight. Solid vertical lines indicate midnight, dash vertical lines indicate noon.

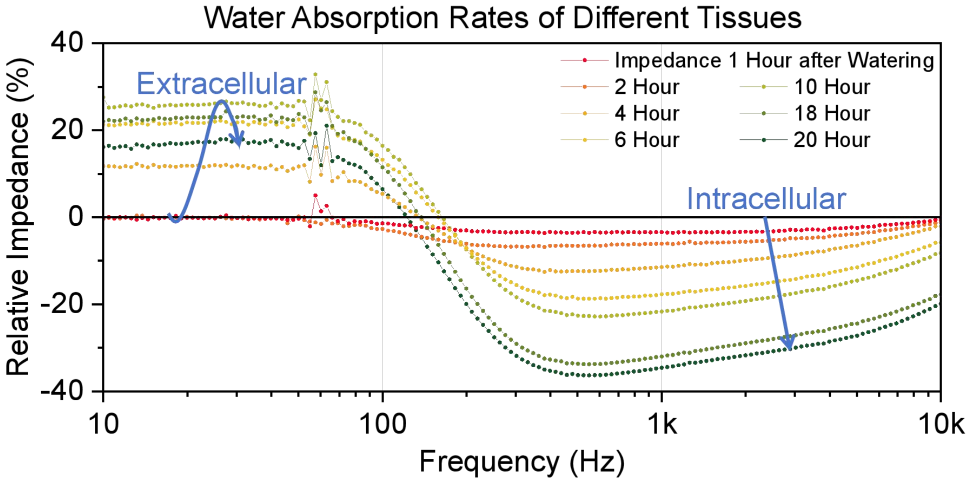

**Figure S10. Frequency-dependent impedance dynamics during water uptake.** Within 20 hours following irrigation, relative impedance ($\Delta Z/Z_0$) changes vary across frequencies, indicating differential water uptake dynamics among leaf extracellular and intracellular compartments.

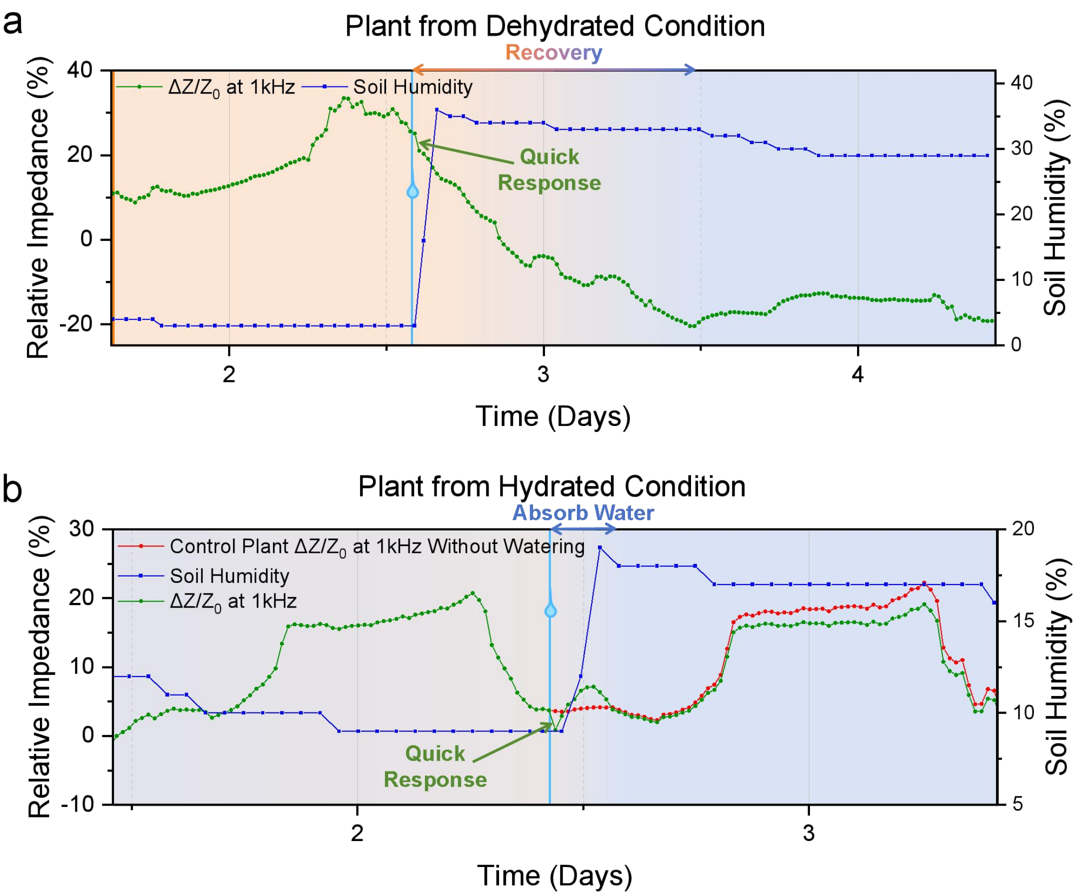

**Figure S11. Long-term dynamic monitoring of leaf impedance under different hydration states. a,** Close-up view of Figure 2c showing the 24 h preceding and 48 h following an irrigation event. A rapid impedance decrease occurs immediately after irrigation, followed by approximately one day of recovery. The water drop icon indicates the irrigation event, and orange vertical lines denote visually observable water stress (leaf curling). Semi-transparent orange and blue shading represent periods of water stress and full hydration, respectively. **b,** Leaf impedance and soil humidity under hydrated conditions. Water absorption persists for approximately 5 hours following irrigation. The red curve represents a non-irrigated control plant. Because the two datasets originate from different plants, baseline impedance values differ. For visual comparison, a constant offset was applied to the control curve beginning at the irrigation time to align baselines; this adjustment does not affect the temporal response dynamics.

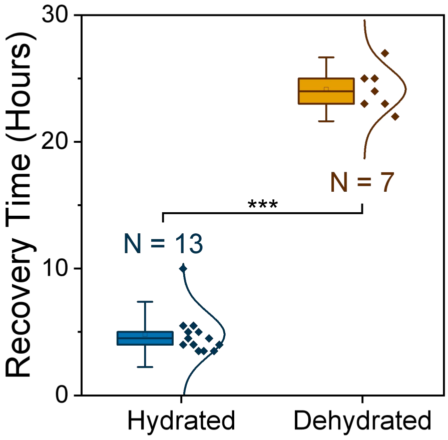

**Figure S12. Comparison of recovery times under hydrated and drought-stressed conditions.** Recovery time was defined as the interval between irrigation and impedance return to baseline. Hydrated plants (N = 13) recovered significantly faster than drought-stressed plants (N = 7). The difference in recovery time was statistically significant ($p = 5.05\times10^{-12}$).

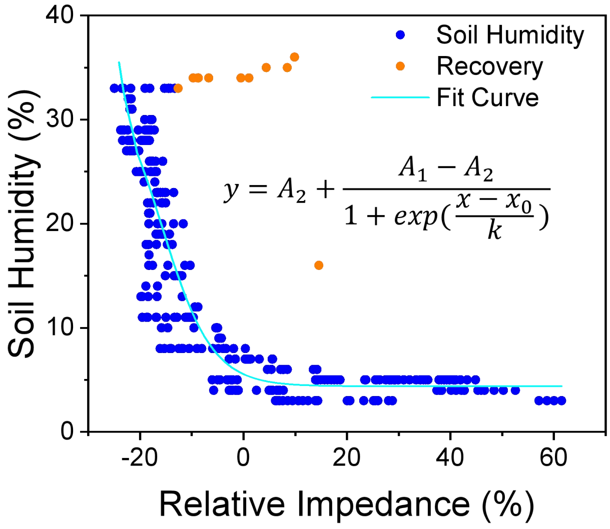

**Figure S13. Relationship between leaf impedance and soil humidity.** Orange points indicate the active recovery phase during water uptake, while blue points represent steady-state conditions. Recovery-phase data were excluded from curve fitting to avoid bias from transient dynamics. A logistic fit captures the nonlinear relationship between soil moisture and leaf hydration state. Logistic model parameters: $A_1 = 4.388$, $A_2 = 35.335$, $x_0 = -15.832$, $k = -4.879$.

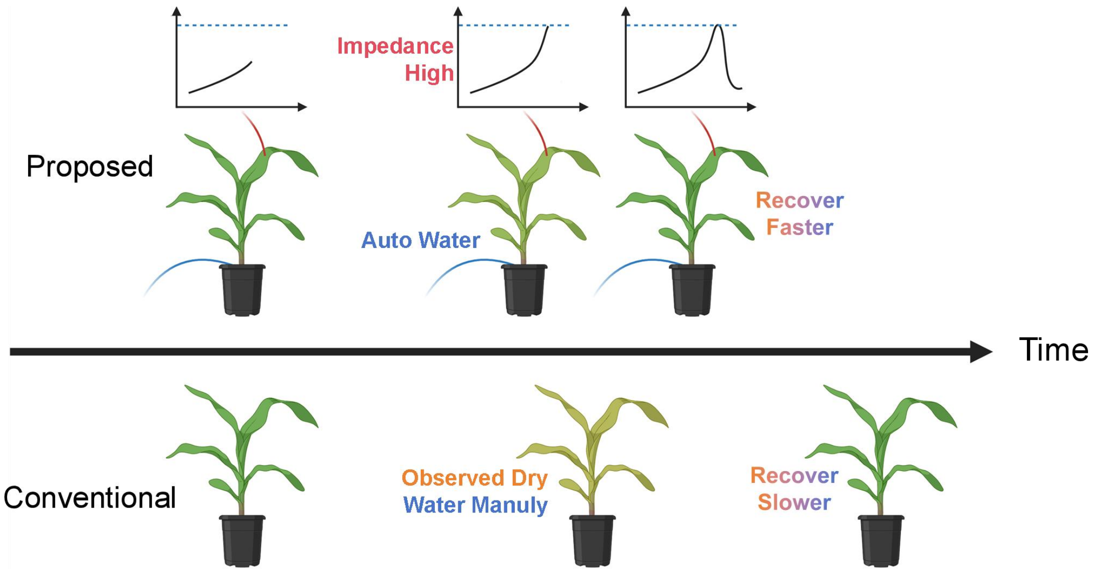

**Figure S14. Conceptual illustration of irrigation management enabled by impedance monitoring.** In the upper diagram, crops are equipped with FGS linked to an automated irrigation system. When impedance rises beyond a threshold, indicating early signs of dehydration, water is delivered preemptively, allowing for faster recovery. In contrast, the lower diagram shows conventional practice in which irrigation is performed after visible leaf curling, indicating more severe dehydration and resulting in slower recovery.

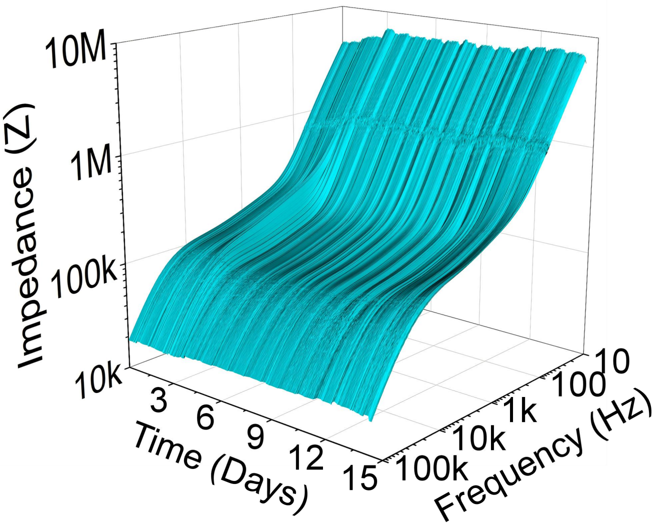

**Figure S15. Continuous impedance monitoring across the large frequency range (10 Hz–100 kHz) over 14 days**.

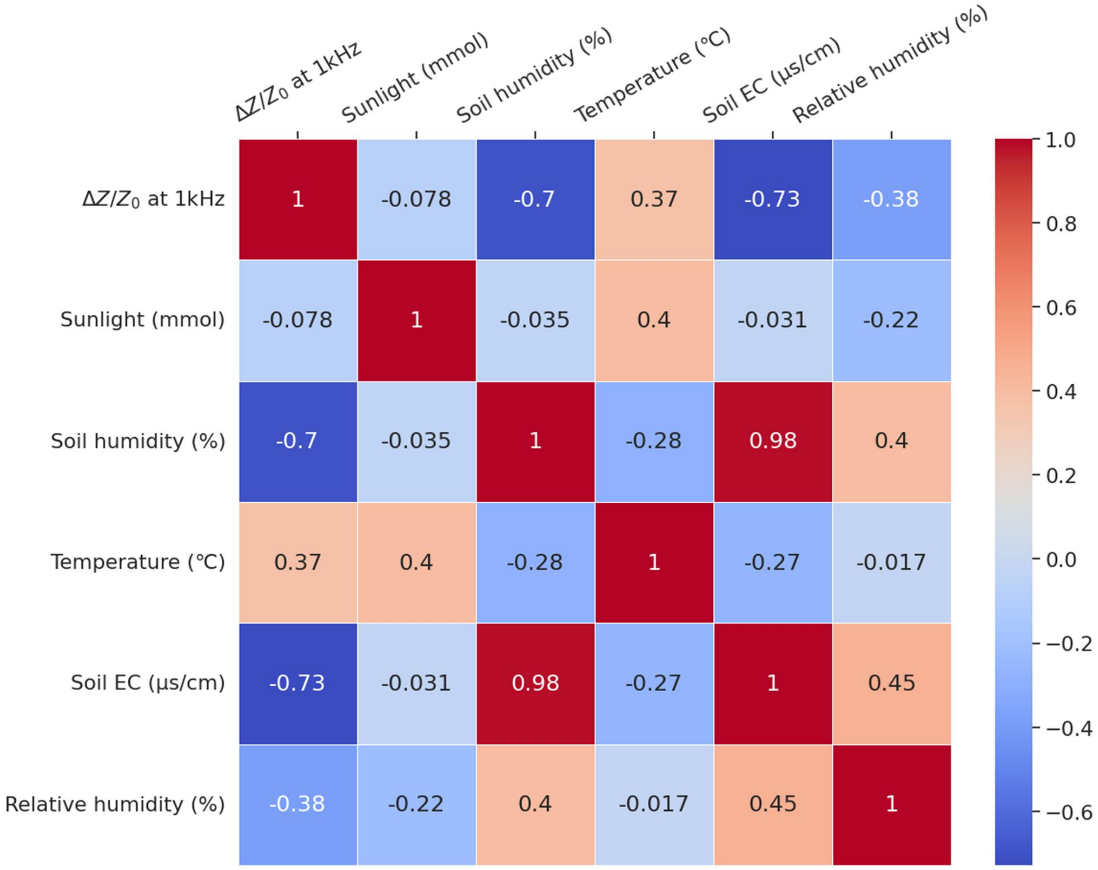

|  | ΔZ/Z₀ at 1kHz | Sunlight (mmol) | Soil humidity (%) | Temperature (°C) | Soil EC (μs/cm) | Relative humidity (%) |
|---|---|---|---|---|---|---|
| ΔZ/Z₀ at 1kHz | 1 | -0.078 | -0.7 | 0.37 | -0.73 | -0.38 |
| Sunlight (mmol) | -0.078 | 1 | -0.035 | 0.4 | -0.031 | -0.22 |
| Soil humidity (%) | -0.7 | -0.035 | 1 | -0.28 | 0.98 | 0.4 |
| Temperature (°C) | 0.37 | 0.4 | -0.28 | 1 | -0.27 | -0.017 |
| Soil EC (μs/cm) | -0.73 | -0.031 | 0.98 | -0.27 | 1 | 0.45 |
| Relative humidity (%) | -0.38 | -0.22 | 0.4 | -0.017 | 0.45 | 1 |

**Figure S16. Correlation heatmap between leaf impedance and environmental parameters.** Pearson correlation coefficients quantify linear associations among impedance ($\Delta Z/Z_0$ at 1 kHz), sunlight intensity, soil humidity, temperature, soil electrical conductivity (EC), and relative humidity. Coefficients greater than 0.5 are indicative of strong positive relationships, whereas values below -0.5 are indicative of strong negative relationships.

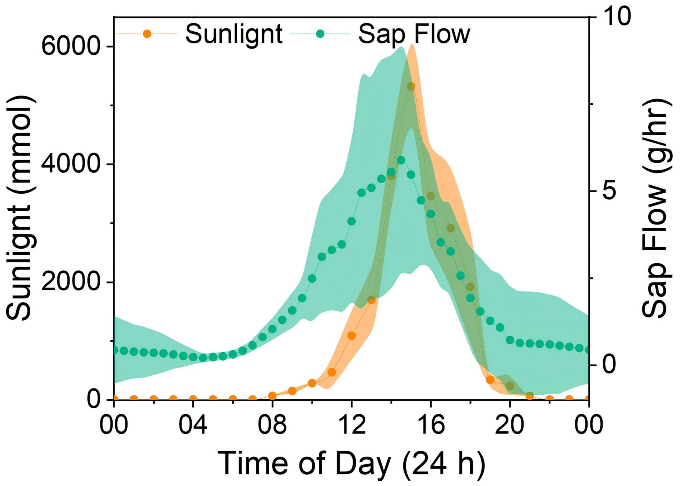

**Figure S17. Diurnal patterns of sunlight intensity and sap flow.** Twenty-day averaged 24-hour profiles show strong alignment between sap flow and sunlight intensity. Solid lines represent means, and semitransparent regions represent ± standard deviation (SD).

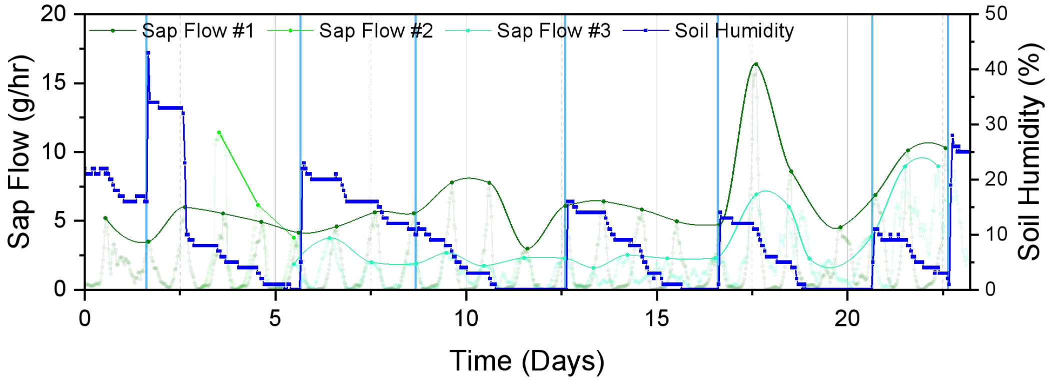

**Figure S18. Sap flow response to irrigation events.** Semi-transparent green curves show real-time sap flow, while solid green lines indicate daily peak values. Light blue vertical lines denote irrigation timing. Sap flow increases typically occur on the following day, indicating delayed hydraulic adjustment.

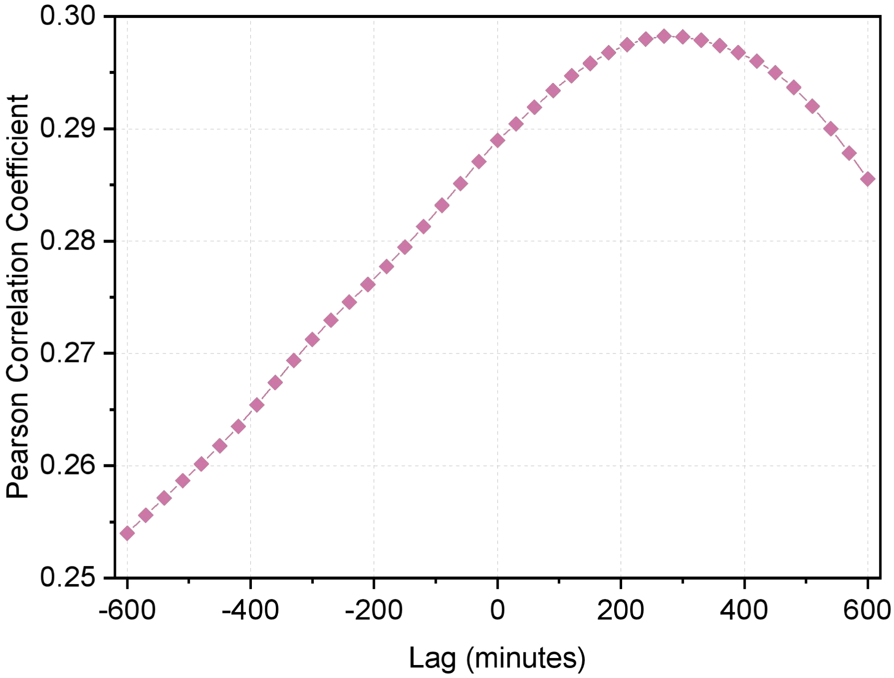

**Figure S19. Lagged correlation between sap flow and leaf impedance.** Pearson correlation coefficients (r) between sap flow and impedance are plotted for lag times from -600 to +600 minutes. Positive lag values indicate sap flow shifted forward in time. The peak correlation at ~4.5 hours indicates that increases in sap flow precede decreases in impedance.

**Table S1. Examples of emerging plant hydration monitoring sensors.**

| *Study Reference* | *Measured Quantity* | *Measurement Method* | *Sensor Materials* | *Sensor Thickness* | *Sensor Weight* | *Invasiveness* | *Continuous Monitoring Duration* |
|---|---|---|---|---|---|---|---|
| *This Work* | Intra-/Extracellular LWC | 4-Probe Impedance | 2 Layer Graphene | < 300 nm | < 0.1 mg | Non-Invasive | 16 Days |
| [11] | LWC | 4-Probe Impedance | Aluminum Foil | -- | -- | Invasive | 2 Days |
| [7] | Leaf Surface RH | DC Resistance | LIG | -- | -- | Invasive | 16 Days |
| [24] | Leaf Surface RH | Capacitance | LIG and GO | -- | -- | Invasive | 11 Days |
| [25] | Leaf Electrical Potential | Capacitance | Polymer + CNT | 50 um | -- | Non-Invasive | 1 Month |
| [5] | Leaf Surface PWC and RH | 2-Probe Impedance | GO | -- | -- | Invasive | 4000 Seconds |
| [6] | Leaf Surface RH | DC Resistance | GO | -- | -- | Invasive | Yes |
| [30] | Leaf Hydration | Conductance | Graphene | < 0.3 um | 9 mg | Non-Invasive | 8 Days |
| [26] | Leaf Surface RH | Voltage | GO | 10 um | -- | Invasive | No |
| [9] | LWC | THz Waves | -- | -- | -- | Non-Invasive | -- |
| [8] | LWC | THz Waves | -- | -- | -- | Non-Invasive | -- |
| [27] | Sap Flow Rate | Temperature | Cu/Pt | -- | 240 mg | Non-Invasive | 16 Days |
| [28] | Leaf Surface Water Content | 2-Probe Impedance | Cu/SWCNT | 30 um | 17 mg | Non-Invasive | 1 Day |
| [29] | Electrophysiology | 2-Probe Impedance | EPC Thermogel | 1 mm | -- | Non-Invasive | -- |

## Supplementary Methods: Statistical Analysis

Statistical analyses were performed in Python using SciPy and statsmodels. Sample sizes (N) refer to independent biological replicates and are reported in figure legends.

Statistical comparisons between two independent groups were performed using Welch's two-tailed t-test, which does not assume equal variances. Statistical significance was defined at $\alpha = 0.05$. p-values $\geq 0.001$ are reported exactly; values $<0.001$ are reported as $p < 0.001$. Graphical annotations use the following convention: * ($p < 0.05$), ** ($p < 0.01$), *** ($p < 0.001$), and n.s. (not significant) for $p \geq 0.05$.

## Supplementary References

1. Zeng, S. *et al.* Ultrafast response of self-powered humidity sensor of flexible graphene oxide film. *Mater. Des.* **226**, 111683 (2023).
2. Lu, Y. *et al.* Multimodal Plant Healthcare Flexible Sensor System. *ACS Nano* **14**, 10966–10975 (2020).
3. Lan, L. *et al.* One-step and large-scale fabrication of flexible and wearable humidity sensor based on laser-induced graphene for real-time tracking of plant transpiration at bio-interface. *Biosens. Bioelectron.* **165**, 112360 (2020).
4. Electrical and humidity-sensing properties of reduced graphene oxide thin film fabricated by layer-by-layer with covalent anchoring on flexible substrate - ScienceDirect. https://www.sciencedirect.com/science/article/pii/S0925400514004365?pes=vor#bib0225.
5. Li, D., Li, G., Li, J. & Xu, S. Wearable Crop Sensor Based on Nano-Graphene Oxide for Noninvasive Real-Time Monitoring of Plant Water. *Membranes* **12**, 358 (2022).
6. Oren, S., Ceylan, H., Schnable, P. S. & Dong, L. High-Resolution Patterning and Transferring of Graphene-Based Nanomaterials onto Tape toward Roll-to-Roll Production of Tape-Based Wearable Sensors. *Adv. Mater. Technol.* **2**, 1700223 (2017).
7. Yin, S., Ibrahim, H., Schnable, P. S., Castellano, M. J. & Dong, L. A Field-Deployable, Wearable Leaf Sensor for Continuous Monitoring of Vapor-Pressure Deficit. *Adv. Mater. Technol.* **6**, 2001246 (2021).
8. Baldacci, L. *et al.* Non-invasive absolute measurement of leaf water content using terahertz quantum cascade lasers. *Plant Methods* **13**, 51 (2017).
9. Li, R., Lu, Y., Peters, J. M. R., Choat, B. & Lee, A. J. Non-invasive measurement of leaf water content and pressure–volume curves using terahertz radiation. *Sci. Rep.* **10**, 21028 (2020).
10. Miccoli, I., Edler, F., Pfnür, H. & Tegenkamp, C. The 100th anniversary of the four-point probe technique: the role of probe geometries in isotropic and anisotropic systems. *J. Phys. Condens. Matter* **27**, 223201 (2015).
11. Serrano-Finetti, E., Castillo, E., Alejos, S. & León Hilario, L. M. Toward noninvasive monitoring of plant leaf water content by electrical impedance spectroscopy. *Comput. Electron. Agric.* **210**, 107907 (2023).
12. Scoffoni, C. *et al.* The Causes of Leaf Hydraulic Vulnerability and Its Influence on Gas Exchange in Arabidopsis thaliana1[OPEN]. *Plant Physiol.* **178**, 1584–1601 (2018).
13. Blackman, C. J., Brodribb, T. J. & Jordan, G. J. Leaf hydraulics and drought stress: response, recovery and survivorship in four woody temperate plant species. *Plant Cell Environ.* **32**, 1584–1595 (2009).
14. Brodribb, T. J. & Cochard, H. Hydraulic Failure Defines the Recovery and Point of Death in Water-Stressed Conifers. *Plant Physiol.* **149**, 575–584 (2009).
15. Abid, M. *et al.* Improved tolerance to post-anthesis drought stress by pre-drought priming at vegetative stages in drought-tolerant and -sensitive wheat cultivars. *Plant Physiol. Biochem.* **106**, 218–227 (2016).
16. Caldeira, C. F. *et al.* A Hydraulic Model Is Compatible with Rapid Changes in Leaf Elongation under Fluctuating Evaporative Demand and Soil Water Status. *Plant Physiol.* **164**, 1718–1730 (2014).
17. MEASUREMENT OF SAP FLOW DYNAMICS THROUGH THE TOMATO PEDUNCLE USING A

NON-INVASIVE SENSOR BASED ON THE HEAT FIELD DEFORMATION METHOD | International Society for Horticultural Science. http://www.actahort.org/books/991/991_50.htm.

18. Nadezhdina, N., Vandegehuchte, M. W. & Steppe, K. Sap flux density measurements based on the heat field deformation method. *Trees* **26**, 1439–1448 (2012).

19. Schreel, J. D. M., Van de Wal, B. A. E., Hervé-Fernandez, P., Boeckx, P. & Steppe, K. Hydraulic redistribution of foliar absorbed water causes turgor-driven growth in mangrove seedlings. *Plant Cell Environ.* **42**, 2437–2447 (2019).

20. Vandegehuchte, M. W. & Steppe, K. Sapflow+: a four-needle heat-pulse sap flow sensor enabling nonempirical sap flux density and water content measurements. *New Phytol.* **196**, 306–317 (2012).

21. Schäfer, K. V. R., Oren, R. & Tenhunen, J. D. The effect of tree height on crown level stomatal conductance. *Plant Cell Environ.* **23**, 365–375 (2000).

22. Phillips, N., Nagchaudhuri, A., Oren, R. & Katul, G. Time constant for water transport in loblolly pine trees estimated from time series of evaporative demand and stem sapflow. *Trees* **11**, 412–419 (1997).

23. Kireev, D., Kampfe, J., Hall, A. & Akinwande, D. Graphene electronic tattoos 2.0 with enhanced performance, breathability and robustness. *Npj 2D Mater. Appl.* **6**, 46 (2022).

24. Lan, L. *et al.* One-step and large-scale fabrication of flexible and wearable humidity sensor based on laser-induced graphene for real-time tracking of plant transpiration at bio-interface. *Biosens. Bioelectron.* **165**, 112360 (2020).

25. Wong, Y. J. *et al.* Adaptable thermoresponsive polymer for long-term electrical coupling in plant electrophysiology monitoring. *Sci. Adv.* **12**, eady1400 (2026).

26. Zeng, S. *et al.* Ultrafast response of self-powered humidity sensor of flexible graphene oxide film. *Mater. Des.* **226**, 111683 (2023).

27. Cohabiting Plant-Wearable Sensor In Situ Monitors Water Transport in Plant - Chai - 2021 - Advanced Science - Wiley Online Library. https://advanced.onlinelibrary.wiley.com/doi/10.1002/advs.202003642.

28. Zhao, Y. *et al.* Multifunctional Stretchable Sensors for Continuous Monitoring of Long-Term Leaf Physiology and Microclimate. *ACS Omega* **4**, 9522–9530 (2019).

29. Luo, Y. *et al.* A Morphable Ionic Electrode Based on Thermogel for Non-Invasive Hairy Plant Electrophysiology. *Adv. Mater.* **33**, 2007848 (2021).

30. Misra, U. *et al.* Graphene In-Sensor Compute Device for Plant Hydration Monitoring. *Nano Lett.* **26**, 2432–2440 (2026).